scientific reports

OPEN

The numerical study of pressure and temperature effects on mechanical properties of baghdadite-based nanostructure: molecular dynamics simulation

Qun Liu[1✉], Olga Bykanova[2], Ravil Akhmadeev[3], Shaghayegh Baghaie[4✉], Maboud Hekmatifar[4], Ahmadreza Arefpour[5], Roozbeh Sabetvand[6] & Vitaliy Borisov[7]

Bioceramics have been commonly implemented to replace and restore hard tissues such as teeth and bones in recent years. Among different bioceramics, Baghdadite (BAG) has high bioactivity due to its ability to form apatite and stimulate cell proliferation. So, this structure is used widely for medical applications to treat bone-based diseases. Physically, we expect changes in temperature and pressure to affect the Baghdadite-based nanostructure's mechanical behaviour. So, in this computational study, we report the pressure/temperature effect on Baghdadite matrix with nanoscale size by using Molecular Dynamics (MD) approach. To this end, physical values like the total energy, temperature, final strength (FS), stress–strain curve, potential energy, and Young's modulus (YM) are reported. Simulation results indicated the mechanical properties of Baghdadite (BAG) nanostructure weakened by temperature and pressure increase. Numerically, the FS and YM of the defined structure reach 131.40 MPa/159.03 MPa, and 115.15 MPa/139.72 MPa with temperature/pressure increasing. Therefore, the increase in initial pressure and temperature leads to a decrease in the mechanical properties of nanostructures. These results indicate the importance of the initial condition in the Baghdadite-based nanostructures' mechanical behaviour that must be considered in clinical applications.

Bioceramics and Bioglasses are environmentally friendly ceramic materials[1]. Bioceramics are in the collection of bio substances[2,3]. Bioceramics are biocompatible from the ceramic oxides to the rest of the absorbable substances that the body finally replaces after helping to repair[4,5]. Today, bioceramics are utilized in a variety of medical methods. Bioceramics are common in engineered bioreactors or extracorporeal circulation systems [6]. They are useful because they are ineffective in the body of a human, and their stiffness and corrosion resistance make them beneficial for bone and tooth substitution[7,8]. Bioceramics samples are widely used to repair and substitute stiff tissues such as bones, teeth, and mineral matrices. Due to their physical and chemical similarity to these types of tissues, bioceramics can be used in calcium silicate-based structures due to their high ability to form apatite and stimulate cell proliferation and biodegrade at appropriate rates regenerate hard tissue[9–12]. Silica-based porous bioceramic scaffolds are very important for the remedy of bone deficiencies. One of the problems of these frameworks is their intrinsic fragile essence and high degradation rate. The use of biodegradable and bioactive polymer

[1]Harbin University, Harbin 150080, Heilongjiang, China. [2]Department of Higher Mathematics, Plekhanov Russian University of Economics, Stremyanny lane, 36, Moscow, Russia 117997. [3]Department of Finance and Prices, Plekhanov Russian University of Economics, Stremyanny lane, 36, Moscow, Russia 117997. [4]Department of Mechanical Engineering, Khomeinishahr Branch, Islamic Azad University, Khomeinishahr, Iran. [5]Advanced Materials Research Center, Department of Materials Engineering, Najafabad Branch, Islamic Azad University, Najafabad, Iran. [6]Department of Energy Engineering and Physics, Faculty of Condensed Matter Physics, Amirkabir University of Technology, Tehran, Iran. [7]Department of Propaedeutics of Dental Diseases, Sechenov First Moscow State Medical University, Moscow, Russia. ✉email: liuqun9992021@163.com; shaghaieghbaghaie@yahoo.com

coatings on the surface of the framework has led to improved mechanical attributes and the ability to rein their degradation rate. Sadeghzadeh et al.[13] provided net Baghdadite (BAG) frameworks at different temperatures (1250–1350 °C), and optimal mechanical and physical attributes were obtained under conditions (temperature 1350° C and a density of 65 MPa) with spherical morphology. Schumacher et al. [14] performed a study to develop the potential usages of BAG in biomedicine. They showed that bulk BAG ceramics had the maximum mechanical attributes at 1400 °C, and at this temperature, fracture toughness and hardness were 30 and 12% higher than hydroxyapatite (HA). Structurally, BAG ($Ca_3Zr(Si_2O7)O_2$ or $Ca_3ZrSi_2O_9$) is a silicate mineral of calcium zirconium, which has been detected in melilite skin contact with banded diorite from the Qala-Dizeh area, North East of Iraq, and reported in 1986[11]. After this basis, the experimental investigations showed this structure includes ZrO_2 (27.00%), SiO_2 (29.26%), TiO_2 (2.11%), Al_2O_3 (0.03%), Fe_2O_3 (0.11%), MgO (0.05%), Na_2O (0.02%) and CaO (41.44%) units[15]. Unit cell factors of natural BAG are a = 10.432 Å, b = 10.163 Å, c = 7.356 Å, β = 90.96°, and the symmetry of the crystal is defined by the space group P21/a. Mechanical properties of BAG such as Young's modulus (YM) and Poisson's ratio of net BAG (bulk sample), are as Es = 126 GPa and v_s = 0.23 respectively[11]. Technically, one of the most important applications of this bioceramic is the treatment of bone injuries, which this performance arises from their mechanical behavior[9,16].

Recently, BAG has been the focus of many academic researchers and has been extensively studied in porous frameworks, coatings, bone cement and void fillers, microspheres and nanoparticles (NPs), orthopaedic, dental and maxillofacial usages[11,17,18]. Arefpour et al.[19] fabricated and investigated the laboratory method of BAG bioceramic nanoparticles ($Ca_3ZrSi_2O_9$) for clinical uses. NPs were examined by X-ray diffraction, field emission scanning electron microscopy, energy-dispersive X-ray spectroscopy, distribution of particles size via laser beam scatter method, Fourier transforms infrared spectroscopy, and transmission electron microscopy. Soleymani et al.[20] presented a polymer-based composite to enhance its corrosion resistance, bioactivity and biocompatibility. In this examination, anodized AZ91 alloy was covered with a polymer matrix composite prepared of polycaprolactone/chitosan (PCL/Ch) with various BAG percentages. The results showed that the nanopolymer-ceramic coating increases corrosion resistance and decreases current density. By physical vapour deposition coupled with electrophoretic deposition, Bakhsheshi et al.[21] prepared zinc oxide (ZnO) and ZnO/BAG on the surface of Mg alloy. The results demonstrated ZnO/BAG is a promising coating for orthopaedic usages of biodegradable Mg alloys seeing its excellent antibacterial activities and high corrosion resistance. Pham et al.[22] investigated the mechanical and biological attributes of BAG coatings synthetic on Ti_6Al_4V substrating using hybrid water-stabilized plasma spray. Mechanical tests showed that the BAG coating provides higher rigidity, elastic modulus and better resistance to scratches and abrasion. Khandan et al.[23] presented an investigation of the effect of spark plasma sintering and BAG powder on the mechanical attributes of hydroxyapatite. In this examination, a new nanocomposite based on bioceramics like Natural HA and BAG was sintered using the spark plasma sintering method. In other experimental research, Karimi et al.[24] covered BAG on the surface treated with poly L-lactic acid (PLLA) plasma and assessed the bony potential of principal mesenchymal cells. The outcomes demonstrated the amount of calcium and current cells' alkaline phosphatase (ALP) activity on PLLA–BAG nanofibers were higher than that of texture culture polystyrenes. Gene statement examination displayed that PLLA–BAG had impressively contained osteogenesis linked genes.

Computer simulations play a substantial role in accurately solving and interpreting the results of some unknown problems in statistical mechanics, structural issues, and the activity of biomechanical molecules; Problems that may not be solvable by other methods or may be difficult or can only be solved by approximate methods. On the one hand, simulations provide a tool for measuring the validity of the theories or models proposed. Technically, outcomes of the simulations are directly comparable to the results of real experiments. Because molecular systems generally comprise large numbers of particles, it is impossible to determine the characteristics of mixed systems analytically. Molecular dynamics (MD) simulation explains this problem using computational procedures. MD systematically examines the relationships between molecule structure, molecule motion, and molecular functions[25–27]. Previous studies show that the influence of primary temperature (in the range of 250–350 K) and primary pressure (in the range of 0–10 bar) on the mechanical behaviour of BAG-based nanostructures has not been investigated. Due to the high performance of the MD in investigating the mechanical attributes of nanostructures, in the present work, the influences of initial temperature and pressure variation on the mechanical conduct of the pristine BAG matrix with the nanoscale size is reported using the MD method. According to our knowledge, the MD is utilized for the first time to describe the BAG's mechanical/atomic behaviour at different temperatures and pressures. The MD simulations can be described the time evolution of BAG with atomic accuracy. Due to the importance of nanostructures' strength and mechanical properties, it expects these reliable results to be considered in BAG-based nanostructures' clinical applications to improve the efficiency of common treatment methods in dental, bone repair, and other similar purposes.

MD simulation details

In this computational research, the MD approach describes the temperature and pressure effects on the BAG's mechanical performance. The MD simulations are important approaches for understanding the physical properties of the nanostructures[28–30]. Historically, this type of simulation was expanded in the late 1970s for the first time[31] to dominate the computational constraints using suitable accesses according to Newtonian formalism to define the evolution of atomic structures, thereby reducing the complication of the atomic system. This computational method describes the time evolution of different atomic arrangements. For this purpose, Newton's equations are solved as below[32]:

Element	σ (Å)	ε (kcal/mol)
O	3.500	0.060
Ca	3.399	0.238
Zr	3.124	0.069
Si	4.295	0.402

Table 1. The ε and σ constant parameters for LJ formalism and reaction of various atoms in the MD simulation box[37].

$$F_i = \sum_{i \neq j} F_{ij} = m_i \frac{d^2 r_i}{dt^2} \tag{1}$$

From this equation, the atomic momentum P_i can be formulated as relation (2) [ ],

$$P_i = m_i v_i \tag{2}$$

Then, the total energy (E) of structures can be described in the form of Hamiltonian as follow[32],

$$H(r, P) = \frac{1}{2m} \sum_i P_i^2 + V(r_1 + r_2 + \ldots + r_n) = \text{ } \tag{3}$$

Lastly, the Velocity-Verlet approach is applied to describe the atomic evolution considering integrations form of Newton law in the below equations [33–35],

$$r_i(t + \Delta t) = r_i(t) + v_i + \frac{1}{2} a_i(t) \Delta t^2 + O(\Delta t^4) \tag{4}$$

$$v_i(t + \Delta t) = v_i + \frac{a_i(t) + a_i(t + \Delta t)}{2} \Delta t + O(\Delta t^2) \tag{5}$$

In both relations, $v_i(t + \Delta t)$ and $r_i(t + \Delta t)$ are velocity and position of atoms at any time (respectively) and $r_i(t)/v_i(t)$ are the primary quantity of these physical parameters. Theoretically, different collections make an initial condition in MD simulations. In these formalisms, the interatomic potential is an important parameter for results which gain from simulations in the defined initial condition. We use Universal Force Field (UFF) for BAG-based nanostructures simulation[37]. To produce a UFF, parameters are required that include a set of hybridization-dependent atomic bond radii, a set of hybridization angles, van der Waals factors, and a set of effective atomic charges. The potential energy for a molecule of any shape and geometry is presented as the sum of the various interactions of two, three, and four. Potential energy is presented as the sum of bonded and non-bonded interactions[37]:

$$E = E_R + E_\theta + E_\phi + E_\omega + E_{V\,dW} + E_{el} \tag{6}$$

In relation (6), E_R, E_θ, E_ϕ and E_ω represent the bond stretching, bond angle bending, dihedral angle torsion, and inversion terms, respectively. Also, non-bonded interactions comprise van der Waals ($E_{V\,dW}$) and electrostatic (E_{el}). Non-bonded interactions (van der Waals forces) are included in the UFF. In this potential interatomic, the non-bond interaction between different atoms is defined by the Lennard–Jones (LJ) as the following equation[38]:

$$U(r) = 4\varepsilon \left[\left(\frac{\sigma}{r_{ij}} \right)^{12} - \left(\frac{\sigma}{r_{ij}} \right)^6 \right] \quad r < r_c \tag{7}$$

where σ is the distance at which the potential gets zero, ε is the potential well depth, r_{ij} is the distance between various atoms, and r_c is the cut-off radius with a 12 Å value. The Lennard–Jones potential function has been used to calculate the interatomic interaction of Carbon-Hydrogen, Carbon–oxygen, Carbon-Calcium, Carbon- Silicon, Carbon-Zirconium, and Silicon- Zirconium, Calcium- Zirconium, etc. These constant parameters values from the UFF reference paper are presented in Table 1.

The electrostatic interaction is another non-bond parameter in the current study, implemented using the classical Coulomb equation[39]. Furthermore, bonded interactions in the BAG-based nanostructures are defined by an equation of a simple harmonic oscillator for angular and simple interactions[40]. Generally, MD simulation involves the step-by-step numerical resolvent of classical motion relations. Therefore, the forces acting on the atoms must be calculated. These forces come from potential energy derivatives. The potential function can be very intricate when it requires precise representations of atomic interactions inside the system. The intricate nature of these interactions is because of the intricate quantum effects occurring at subatomic levels. To obtain acceptable results in MD-based research, classical interatomic potentials must appropriately accept quantum effects. Typically, the potential formalisms function the experimental observations obtained and modelling and simulation

at the quantum scale[41]. The function of potential for specific types of systems has been widely deliberated. The generic structure of this function can be shown as follows[42]:

$$U(r_1, r_2, ..., r_N) = \sum_i V_1(r_i) + \sum_{i,j>1} V_2(r_i, r_j) + \sum_{i,j>1,k>j} V_3(r_i, r_j, r_k) + ... \tag{8}$$

Here, r is the position vector of the particles, and the V_m function is called the potential of m-particles. The first phase in Eq. (8) indicates the energy obtained from an outer force field like gravity or electrostatic. The second expression represents the dual potential energy between particles, and the third expression is related to the potential of three particles. The function V_1 is called the outer potential, V_2 is called the pair potential, and V_m (m > 2) is called the particle potential. In practice, the second expression is ignored to reduce the volume of numerical simulation calculations. The effect of multi-particle potentials with appropriate degrees of accuracy is included in the pair potentials.

Details of atomic structures simulations with MD approach.   After defining the force field and the atomic modelling process inside the MD box, the conditions under which the BAG is simulated using MD are as follows. In this sector, the atomic arrangement of the BAG-based nanostructure is described in the MD simulation box. The matrix is secured in the middle of the box, and the area around the volume is considered free space. The size of the free space in the equilibrium process must be calmed to adjust the density of the atomic sample to an appropriate value. BAG-based nanostructure equilibrated at a primary condition for t=10 ns. For this purpose time, the step amount is set to 1 fs. NPT ensemble is used in the MD simulation. In this ensemble, 0.01 and 0.1 values are set to damp values of temperature and pressure parameters. Also, the initial condition for the defined atomic structure is $T_0 = 300$ K and $P_0 = 0$ bar, implemented using Nose-Hoover barostat. Also, the type of thermostat used to regulate the temperature in this study is Nose-Hoover[43,44]. Computationally, the MD simulation boxes are 150 Å in x orientation and 50 Å in y and z orientations, and 5400 atoms are described inside the simulation box. Technically, periodic boundary conditions are used in different simulated structures[45]. In this step, total energy and temperature changes are calculated as a function of MD simulation time to present the equilibration trend in the simulated compound.

Details of the tensile test process.   After equilibrium phase detection, the deformation procedure (tensile test) is implemented to the BAG-based sample in the x-direction by an external force, and the mechanical properties are reported. Using this external force, the strain rate was set to 0.0001 s⁻¹ inside the simulation box, and stress outputs were printed every n-time step. Technically, to calculate strain and stress values in our MD study, matrix length in the x-direction and interatomic pressure were calculated at every step. After a mechanical test was done for the atomic matrix at the initial condition, the temperature and pressure change and influence of these physical parameters on the mechanical attributes of the BAG-based sample were reported. The stress-strain curve calculated mechanical attributes like final strength (FS) and YM.

Results

Atomic arrangement of the BAG.   As the first step of the present study, the BAG's atomic arrangement is described inside the MD simulation box. For this computational stage, the matrix is formed in the middle region of the box, as the area around the volume is defined as free space. This free space size relaxed the equilibrium process to set atomic sample density at an appropriate value. Technically, the defined atomic compound in the current study prepared by an internet database and Avogadro package[46]. Figure 1 displays the atomic arrangement for the BAG-based sample inside the MD simulation box, visualized by OVITO software[47].

Equilibrium process.   After the atomic modelling process and MD settings implementation to atomic structure, temperature, total energy, and density variation of the atomic sample are reported[48]. Figure 2 exhibits BAG's total energy and temperature changes in simulation time. The MD outcomes indicated that the defined structure's total energy and temperature reached −2363.66 eV and 300 K. Furthermore, potential energy changes in MD simulation time are reported in Fig. 2c. As shown in this figure, after 10 ns, this physical parameter reaches to −3164.04 eV value. These calculated physical parameters show that the MD time is large enough in the balance procedure, and modelled structures at this time reach physical fixity. Also, the simulated matrix's negative ratio of total energy indicates appropriate matching between atoms' positions and interatomic potential in the present computational study. Also, the density of BAG changes applying the MD time reported in Fig. 3. Our simulations show the density of the atomic matrix converged to a 3.37 g/cm³ value after t = 10 ns. This computation is compatible with prior presents and shows the integrity of our modelling, potential definition, and other MD settings in the present work[49].

Tensile test results.   After equilibrium phase detection, an external force implemented the BAG's tensile test (mechanical deformation). The NPT ensemble is used in the MD simulation box for t = 2 ns in this step. Firstly, we calculate the mechanical behaviour of the bulk sample of the BAG structure. MD outputs for stress and strain parameters are depicted simultaneously in Fig. 4. This figure shows that FS of bulk structure converged to 172.48 GPa, and YM of this sample reached 118.28 GPa after 2 ns. MD results for bulk structure of BAG sample are consistent with previous reports and show our simulation method correctness in current research[50]. Next, a bulk BAG sample was converted to nanostructure one by adding 15 Å vacant space inside the MD box and external force implemented to defined nanostructure.
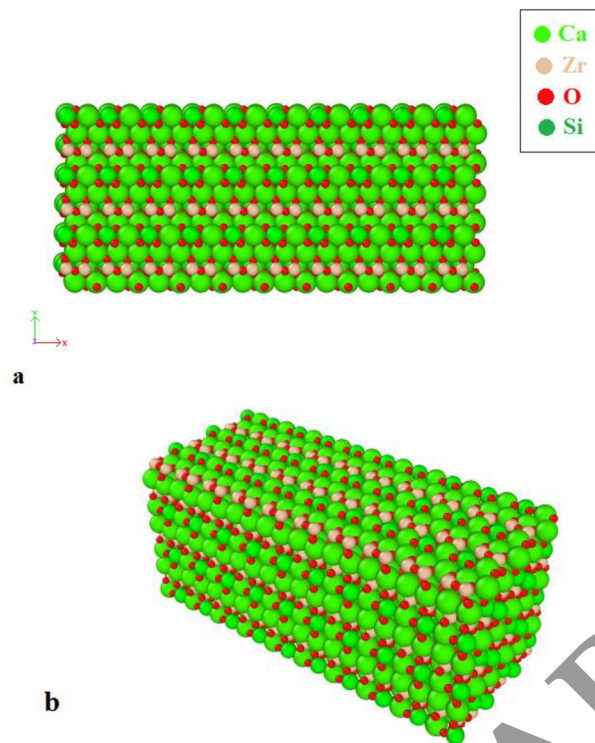
Figure 1. Schematic of modelled BAG-based nanostructure at (**a**) Front and (**b**) Perspective views.

Figure 5a indicates the atomic arrangement of the BAG-based nanostructure before and after the deformation procedure. After performing a mechanical test on the simulated sample, the atoms move away from each other in some areas of the pristine matrix. This atomic evolution causes cracks creation inside the atomic structure, decreasing the mechanical resistance of the simulated nanostructure (see Fig. 5b).

So, by implementing this atomic procedure, mechanical properties of pristine structures like YM and stress–strain curve are represented in Fig. 6. Theoretically, the constants of mechanical like the YM and FS of the BAG-based nanostructure can be calculated from the stress–strain curve as depicted in Fig. 6. In addition, it measures the relationship between axial strain (proportional deformation) and tensile stress sigma (force per unit area) in the linear elastic area of the BAG sample. MD simulations show that the FS and YM of the pristine BAG sample converge to 157.14 and 174.74 MPa, respectively. Physically, this calculation shows the tensile stiffness of the BAG structure. Also, the FS parameter is the maximum stress a substance can tolerate during stretching or pulling before breaking. Computationally, these calculated results are derived from the stress–strain curve. The strain rate during tensile testing significantly affects BAG's mechanical attributes and deformation conduct. Table 2 lists the YM and FS of BAG as a function of various strain rates. MD outputs indicated by strain rate increasing in the mechanical test process, the mechanical strength of defined atomic structure decreases. This mechanical behaviour arises from atomic fluctuation amplitude increasing by strain rate enlarging. Numerically, by strain rate changes from 0.0001 to 0.0005, the FS and YM decrease to 137.11 and 160.10 MPa, respectively. Furthermore, by comparing mechanical outputs of BAG structure in bulk and nano scales, we conclude that the mechanical performance of atomic samples appreciably changes by sample size changes, which this behaviour reported in previous research[50]. In our case study, the mechanical strength of the BAG-based sample decreases by size decreasing. This atomic evolution arises from the attraction force decreasing between various atoms inside the MD simulation box.

Different pressures affect the mechanical performance of BAG-based nanostructure. In the next step of our computational examination, the MD simulations are done at various pressures for describing this physical parameter effect on the BAG's mechanical behaviour. The calculated stress–strain curve of the atomic nanostructure applying initial pressure is related in Table 3 and Fig. 7. From these calculations, it can be said that YM and FS of the BAG sample converge to 131.40 and 115.15 MPa values after the atomic deformation process done at $P_0 = 10$ bar, respectively (see Table 3). The potential energy increases with pressure, leading to more structural instability. Physically, pressure increases in simulated samples and the atom positions get closer, so the repulsive force increases. This atomic force is derived from the Pauli Exclusion formula, which cases that two or more atoms cannot simultaneously occupy the identical quantum state in a defined nanostructure. By repulsive force increasing inside simulated compounds, the atomic constraints in structures are reduced, and the atomic system's FS reaches lower values. Also, this atomic evolution can be presented using potential energy decrease in the box of MD. Numerically, this physical factor changes from −3032.28 to −2600.27 eV using initial pressure changes from 0 to 10 bar, respectively. The description of BAG sample behaviour in high pressures
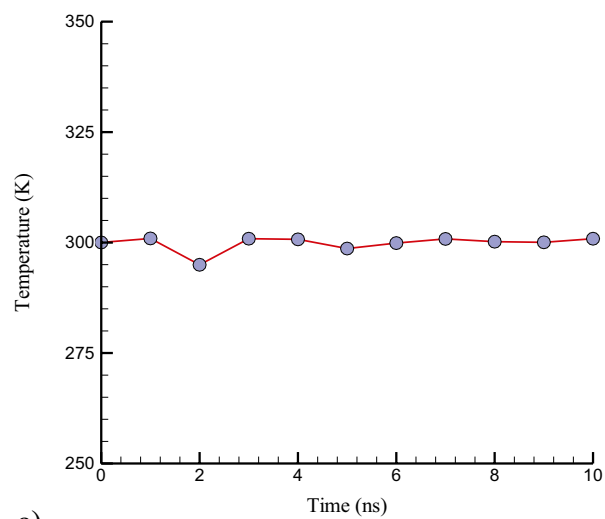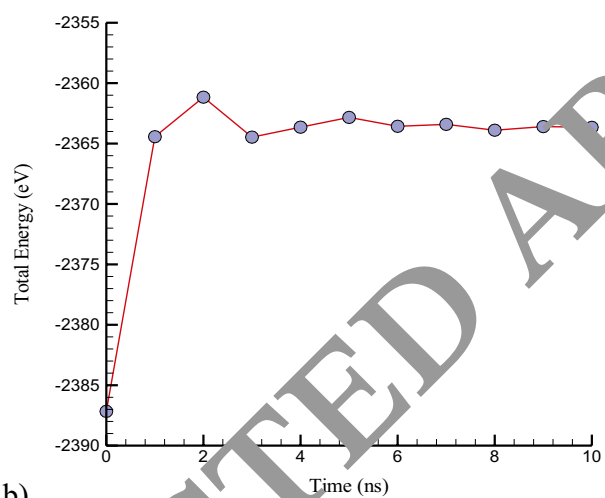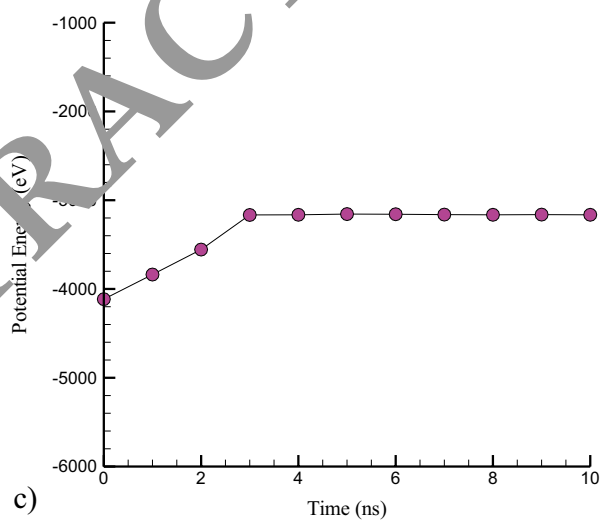
Figure 2. BAG-based nanostructure change's (**a**)temperature, (**b**) total energy, and (**c**) potential energy in terms of MD time at $T_0 = 300$ K and $P_0 = 0$ bar.
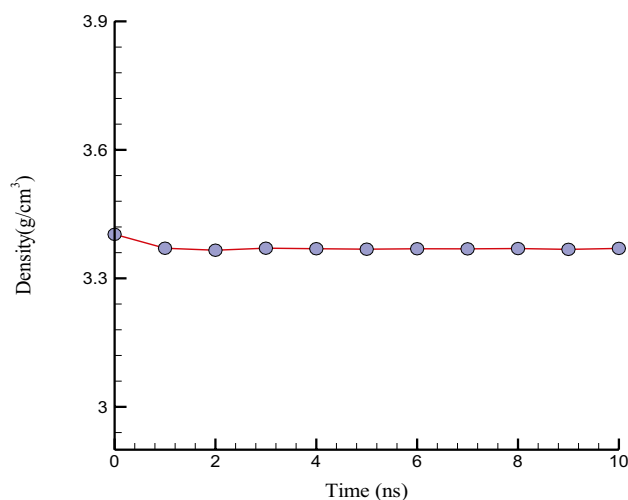
Figure 3. Density of BAG-based nanostructure change in MD simulation time at $T_0 = 300$ K and $P_0 = 0$ bar.
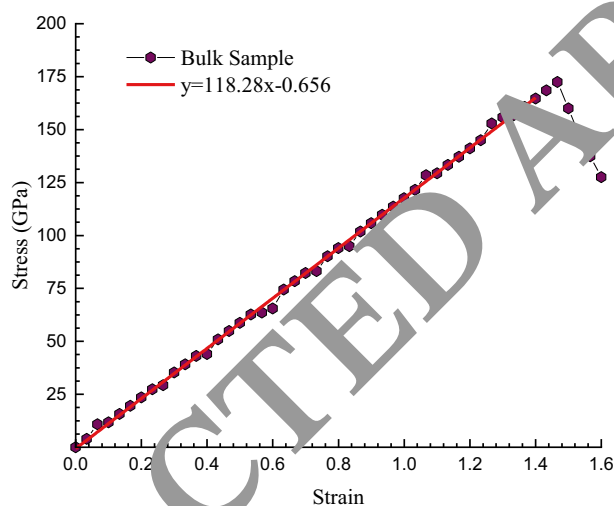

Figure 4. Stress–strain curve of a bulk sample of BAG structure at $T_0 = 300$ K and $P_0 = 0$ bar.

can be helpful for industrial/clinical aims. For describing the mechanical behaviour of atomic matrix in high pressure, this physical parameter increased to 20 bar. MD outputs indicated BAG-based nanostructure physical stability in this pressure. Numerically, by the initial pressure value set at 20 bar, Young's modulus and FS of this compound converged to 111.12 and 103.14 MPa, respectively. The atomic defect is another phenomenon that occurs inside a defined matrix after described mechanical test process. This section describes atomic defects in BAG-based nanostructure by calculating the number of various defects consisting of vacancy, antisite, and dislocation defects. As listed in Table 4, by pressure increasing, the number of atoms involved in vacancy, antisite, and dislocation defects increased and reached 113, 171, and 89 atoms, respectively. These calculated results described the mechanical strength drop in defined atomic compounds more by pressure enlarging.

Furthermore, we concluded physical stability of the defined matrix decreases as atomic defect increases (from Tables 3 and 4). This atomic evolution causes some phenomena such as degradation and corrosion to occur more intensely inside the simulation box. Finally, physical stability decreases cause weakens the mechanical strength of the target nanostructure.

Different temperatures affect the mechanical performance of BAG-based nanostructure.
Temperature changes are another important parameter that can manipulate the mechanical behaviour of various nanostructures. In the final step of this study, the mechanical conduct of BAG-based nanostructure is reported by initial temperature variations from 250 to 350 K. As the temperature in the simulated structures increases, their mobility increases, and atomic displacement amplitude converges to larger ratios. This atomic evolution causes matrixes' physical stability and mechanical strength to decrease. Numerically, as temperature increases from T = 250 to 350 K, the potential energy ratio of the simulated sample changes from −237.70 to
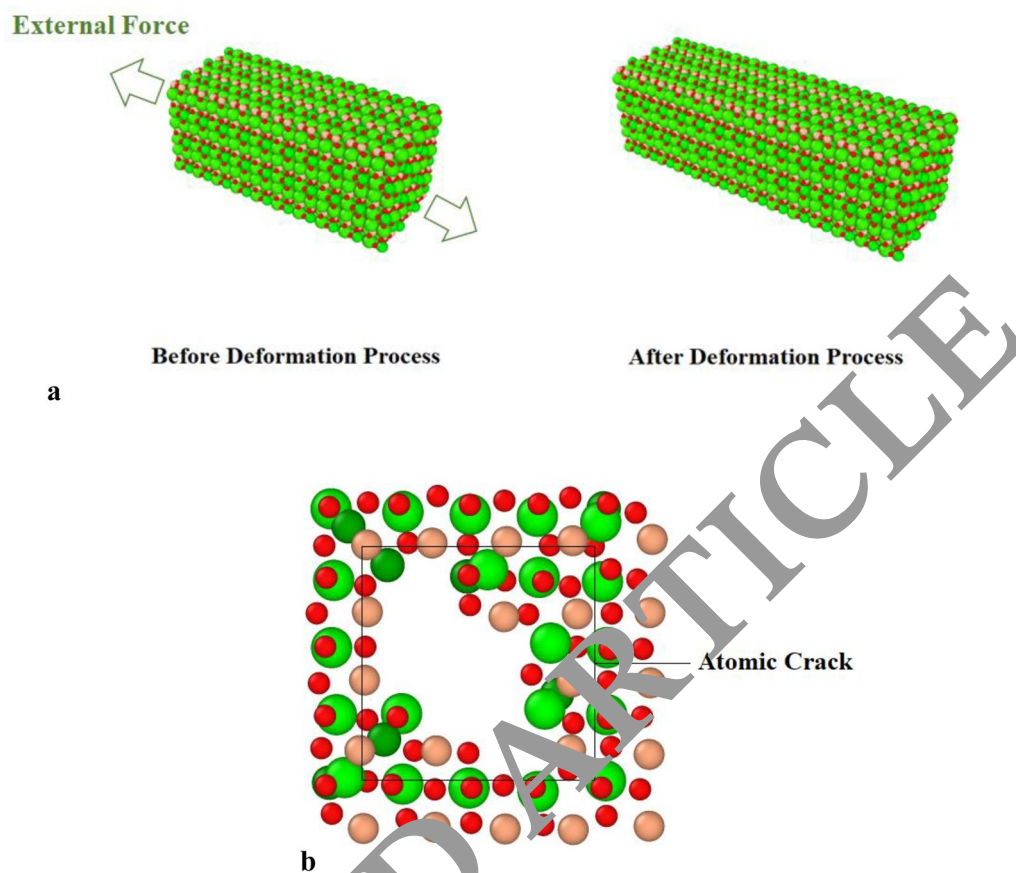
Figure 5. (**a**) The atomic arrangement of BAG-based nanostructure before and after the deformation. (**b**) Snapshot of atomic crack inside (middle region) nanostructure after deformation process done.
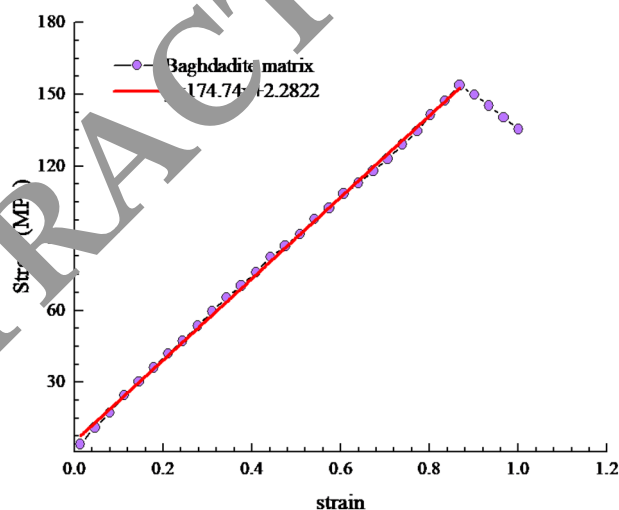

Figure 6. Stress–strain curve of BAG-based nanostructure at $T_0 = 300$ K and $P_0 = 0$ bar.

−2900.39 eV values, respectively. As reported before, the potential energy decrease in the simulated structure shows the attraction force weakening as MD time passing. These physical stability changes directly affect the atomic arrangement's mechanical behaviour. To show this atomic evolution, we depicted the stress–strain curve change of BAG-based nanostructure as a function of initial temperature in Fig. 8. As displayed in this figure, as the temperature increases inside the MD box, the mechanical conduct of the pristine structure significantly changes. Numerically, by temperature enlarging, YM and FS of structures converged to 159.43 and 139.72 MPa,

Strain Rate (s^{-1})	Ultimate Strength (MPa)	Young's Modulus (MPa)
0.0001	153.14	174.74
0.0002	146.66	170.03
0.0003	141.28	168.83
0.0004	139.51	165.47
0.0005	137.11	160.10

Table 2. The BAG's mechanical properties function strain rate in the deformation test process.

Pressure (bar)	Ultimate Strength (MPa)	Young's Modulus (MPa)	Potential Energy (eV)
0	153.14	174.74	−3032.28
1	137.96	157.43	−2848.95
2	131.06	149.55	−2778.33
5	125.16	142.87	−2687.11
10	115.15	131.40	−2600.27

Table 3. The BAG's atomic/mechanical properties function initial pressure in the MD simulation box.
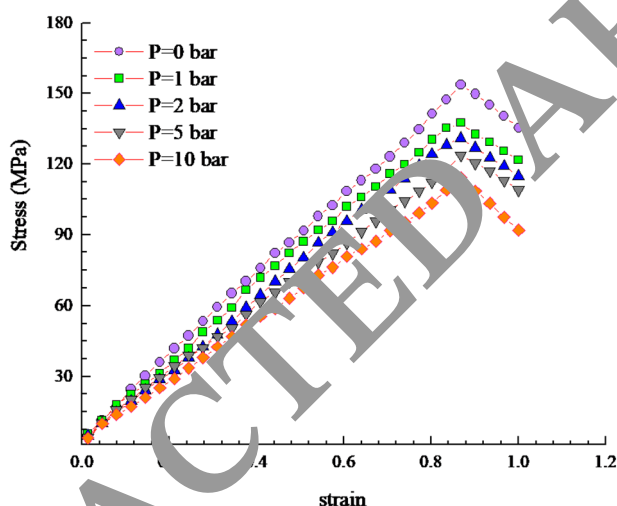

Figure 7. BAG's stress–strain curve functions initial pressure in the MD simulation box.

Pressure (bar)	Vacancy Defect	Anatisite Defect	Dislocation Defect
0	95	155	64
1	103	154	71
2	105	159	76
5	109	166	80
10	113	171	89

Table 4. Changes in the number of involved atoms in vacancy, antisite, and dislocation defects at different pressures.

respectively, as listed in Table 5. We expected these mechanical behaviour changes in simulated structures have an important effect on medical applications, which should be considered in clinical apparatus designing. Similar results were calculated by more initial temperature changes in the defined nanostructure. Numerically, by temperature setting at 10 and 500 K, FS converged to 174.04 and 122.05 MPa, respectively.

Furthermore, BAG's YM reach 197.71 MPa and 148.96 values at T = 10 and 500 K, respectively. These simulation results indicated the atomic stability of BAG-based nanostructure at very low and high temperatures. Similar
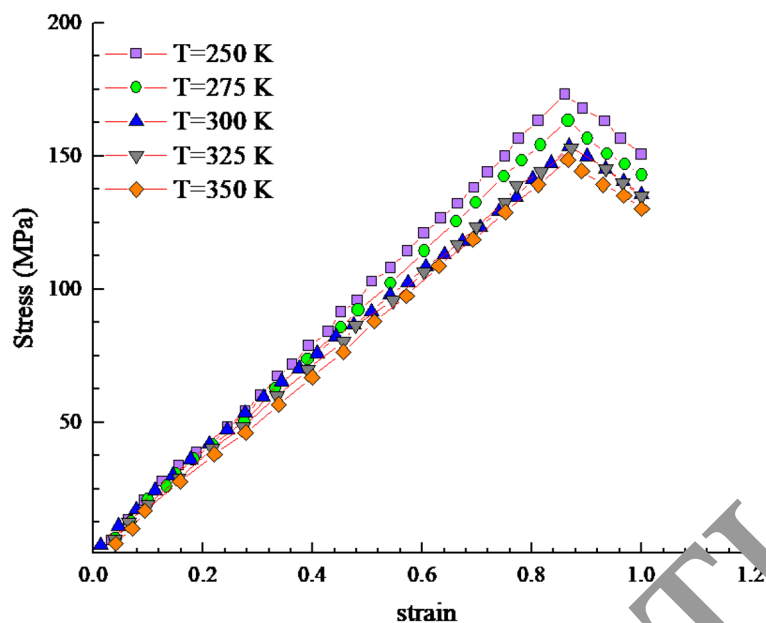
Figure 8. BAG's stress–strain curve in terms of initial temperature in the MD box.

Temperature (K)	Final Strength (MPa)	Young's Modulus ...	Potential Energy (eV)
250	163.72	186.82	−3237.70
275	161.86	184.70	−3131.69
300	153.14	174.74	−3032.28
325	142.81	1...96	−2987.36
350	139.72	159.4...	−2900.39

Table 5. BAG's mechanical/atomic properties in terms of initial temperature in the MD box.

Temperature (K)	Vacancy Defect	Anatisite Defect	Dislocation Defect
250	90	143	55
275	92	148	57
300	98	155	64
325	103	159	72
350	110	166	81

Table 6. Change in the number of involved atoms in vacancy, antisite, and dislocation defects at different temperatures.

to the previous section, the number of atoms involved in vacancy, antisite, and dislocation defects in this step are reported in Table 6. MD results indicated temperature enlarging caused atomic defects increasing inside the defined nanostructure (after mechanical test). Physically, this atomic process occurs by potential energy magnitude decreasing with temperature variations from 250 to 350 K. Numerically, the number of atoms involved in vacancy, antisite, and dislocation defects converged to 110, 166, and 81 atoms (respectively) by temperature enlarging. Finally, according to the results obtained in different parts of this article, it can be said that BAG-based nanostructure can be used in medical applications. This is due to the good stability of this compound and its non-toxicity under standard conditions. On the other hand, MD outputs predicted that the increase in pressure and temperature in the pristine BAG-based nanostructures do not interfere with their mechanical behaviour. Therefore with a high degree of reliability, BAG samples can be used in various medical cases, such as the treatment process of bone diseases.

10

Conclusion

Our research uses the MD method to describe pressure and temperature variation effects on the mechanical behaviour of the BAG samples. Technically, in our simulations, the UFF was utilized in the atomic representation of the pristine BAG sample. After this computational stage, the BAG-based nanostructure implemented a longitudinal deformation process to predict its mechanical properties. The MD outputs indicate that the $t = 10$ ns is enough time for equilibrium procedure detection in defined initial temperature and pressure. Numerically, our outcomes from the BAG's atomic/mechanical analysis in various initial pressure and temperature are as follows:

- BAG's total energy converged to -2363.66 eV values after $t = 10$ ns. This energy convergence showed the atomic stability of the pristine nanostructure in the equilibrium process.
- The MD simulations predicted the quantities of 174.74 MPa and 153.14 MPa for the BAG's YM and FS at $T_0 = 300$ K and $P_0 = 0$ bar.
- By primary pressure enhancement in the MD box (to $P_0 = 10$ bar), the FS and YM of BAG-based nanostructure converged to 131.40 MPa and 115.15 MPa, respectively.
- By initial temperature increasing in the MD simulation box (to $T_0 = 350$ K), the FS and YM of BAG converged to 159.43 MPa and 139.72 MPa, respectively.

From these computational outcomes, we deduce that the primary pressure/temperature of the BAG-based nanostructure is an important parameter for their mechanical behaviour and should be considered for various clinical purposes, such as bone treatment procedures. Also, MD outputs indicated that temperature and pressure variation doesn't disrupt defined compounds' physical stability. This result rises from atomic fluctuation amplitude decreasing by MD time passing. So, we can say that using BAG nanostructure in the treatment of bone-based diseases under various operating conditions doesn't eliminate the stability of the final compound inside the human body, and the repairing procedure is done effectively.

References

1. Huiskes, H., Design, fixation, and stress analysis of permanent orthopedic implants: The hip joint. In *Functional behavior of orthopedic biomaterials. Volume II: Applications*. CRC Press, 1984, pp. 121–162.
2. Shackelford, J. F. Bioceramics(applications of ceramic and glass materials in medicine). In *Materials science forum*, 1999: Trans Tech Publications.
3. Kassinger, R., *Ceramics: From magic pots to man-made bones*. Twenty-First Century Books, 2003.
4. Kinnari, T. J. *et al.* Bacterial adherence to SiO2-based multifunctional bioceramics. *J. Biomed. Mater. Res. Part A: An Off. J. Soc. Biomater. The Jpn. Soc. Biomater. the Austr. Soc. Biomater. Korean Soc. Biomater.* **89**(1), 215–223 (2009).
5. Boch, P. and Niepce, J.-C. *Ceramic Materials: Processes, properties, and applications*. John Wiley & Sons, 2010.
6. Thamaraiselvi, T. & Rajeswari, S. Biological evaluation of bioceramic materials-a review. *Carbon* **24**(31), 172 (2004).
7. Kokubo, T. *Bioceramics and their clinical applications*. Elsevier, 2008.
8. John, Ł, Janeta, M. & Szafert, S. Designing of macroporous magnetic bioscaffold based on functionalized methacrylate network covered by hydroxyapatites and doped with nano-MgFe2O4 for potential cancer hyperthermia therapy. *Mater. Sci. Eng., C* **78**, 901–911 (2017).
9. Plaister, J. R., Jansen, J., de Graaff, R. A. G. & Ijdo, D. J. W. Structure determination of Ca3HfSi2O9 and Ca3ZrSi2O9 from powder diffraction. *J. Solid State Chem.* **115**(2), 464–468 (1995).
10. Al-Hermezi, H. M., McKie, D. & Hall, A. J. Baghdadite, a new calcium zirconium silicate mineral from Iraq. *Mineral. Mag.* **50**(355), 119–123 (1986).
11. Jodati, H., Yilmaz, B. & Evis, Z. Calcium zirconium silicate (baghdadite) ceramic as a biomaterial. *Ceram. Int.* **46**(14), 21902–21909 (2020).
12. Jodati, H., Yilmaz, B., Evis, Z. Calcium zirconium silicate (baghdadite) ceramic as a biomaterial, **46** (14), 21902–21909, (2020).
13. Sadeghzade, S., Emadi, R., Ahmadi, T., and Tavangarian, F. Synthesis, characterization and strengthening mechanism of modified and unmodified porous diopside/baghdadite scaffolds. **228**, 89–97, (2019).
14. Aresta, M., Dibenedetto, A., and Quaranta, E. State of the art and perspectives in catalytic processes for CO2 conversion into chemicals and fuels: The distinctive contribution of chemical catalysis and biotechnology. **343**, 2–45 (2016).
15. Biagioni, C., Bonaccorsi, E., Perchiazzi, N., and Merlino, S. Single crystal refinement of the structure of baghdadite from Fuka (Okayama Prefecture, Japan), (2010).
16. Biagioni, C., Merlino, S., Parodi, G. C. & Perchiazzi, N. Crystal chemistry of minerals of the wöhlerite group from the Los Archipelago, Guinea. *Can. Mineral.* **50**(3), 593–609 (2012).
17. Lu, Z., Wang, G., Roohani-Esfahani, I., Dunstan, C. R. & Zreiqat, H. Baghdadite ceramics modulate the cross talk between human adipose stem cells and osteoblasts for bone regeneration. *Tissue Eng. Part A* **20**(5–6), 992–1002 (2013).
18. Schumacher, T. C. *et al.* Synthesis and mechanical evaluation of Sr-doped calcium-zirconium-silicate (baghdadite) and its impact on osteoblast cell proliferation and ALP activity. *Biomed. Mater.* **10**(5), 055013 (2015).
19. Arefpour, A., Kasiri-Asgarani, M., Monshi, A., Karbasi, S. & Doostmohammadi, A. Baghdadite/Polycaprolactone nanocomposite scaffolds: Preparation, characterisation, and in vitro biological responses of human osteoblast-like cells (Saos-2 cell line). *Mater. Technol.* **35**(7), 421–432 (2020).
20. Soleymani, F., Emadi, R., Sadeghzade, S. & Tavangarian, F. Applying baghdadite/PCL/chitosan nanocomposite coating on AZ91 magnesium alloy to improve corrosion behavior, bioactivity, and biodegradability. *Coatings* **9**(12), 789 (2019).
21. Bakhsheshi-Rad, H. R. *et al.* Synthesis of a novel nanostructured zinc oxide/baghdadite coating on Mg alloy for biomedical application: In-vitro degradation behavior and antibacterial activities. *Ceram. Int.* **43**(17), 14842–14850 (2017).
22. Pham, D. Q. *et al.* Baghdadite coating formed by hybrid water-stabilized plasma spray for bioceramic applications: Mechanical and biological evaluations. *Mater. Sci. Eng.: C* **122**, 111873 (2021).
23. Khandan, A. *et al.* Influence of spark plasma sintering and baghdadite powder on mechanical properties of hydroxyapatite. *Proc. Mater. Sci.* **11**, 183–189 (2015).
24. Karimi, Z. *et al.* Baghdadite nanoparticle-coated poly l-lactic acid (PLLA) ceramics scaffold improved osteogenic differentiation of adipose tissue-derived mesenchymal stem cells. *J. Biomed. Mater. Res., Part A* **107**(6), 1284–1293 (2019).

25. Noorian, H. *et al.* The effects of surface roughness geometry of flow undergoing Poiseuille flow by molecular dynamics simulation. *Heat and Mass Transfer.* **50**(1), 95–104 (2014).

26. Rezaei, M. *et al.* Molecular dynamics study of an electro-kinetic fluid transport in a charged nanochannel based on the role of the stern layer. *Physica A.* **426**, 25–34 (2015).

27. Yan, S. R. *et al.* Prediction of boiling flow characteristics in rough and smooth microchannels using molecular dynamics simulation: Investigation the effects of boundary wall temperatures. *J. Mol. Liq.* **306**, 112937 (2020).

28. Jolfaei, N. A. *et al.* Investigation of thermal properties of DNA structure with precise atomic arrangement via equilibrium and non-equilibrium molecular dynamics approaches. *Comput. Methods Programs Biomed.* **185**, 105169 (2020).

29. Tohidi, M. *et al.* The effect of geometrical parameters, roughness and the number of nanoparticles on the self-diffusion coefficient in Couette flow in a nanochannel by using of molecular dynamics simulation. *Physica B.* **518**, 20–32 (2017).

30. Alipour, P. *et al.* Modeling different structures in perturbed Poiseuille flow in a nanochannel by using of molecular dynamics simulation: Study the equilibrium. *Physica A.* **515**, 13–30 (2019).

31. Haile, J. M., Johnston, I., Mallinckrodt, A. J. & McKay, S. Molecular dynamics simulation: elementary methods. *Comput. Phys.* **7**(6), 625–625 (1993).

32. Rapaport, D. C. *The art of molecular dynamics simulation*. Cambridge university press, (2004).

33. Verlet, L. Computer" experiments" on classical fluids. I. Thermodynamical properties of Lennard-Jones molecules. *Phys. Rev.* **159**(1), 98 (1967).

34. Press, W., Teukolsky, S., Vetterling, W., and Flannery, B. Section 17.4. Second-Order Conservative Equations. *Numerical recipes: The art of scientific computing, 3rd ed., Cambridge University Press, New York,* (2007).

35. Hairer, E., Lubich, C. & Wanner, G. Geometric numerical integration illustrated by the Störmer–Verlet method. *Acta Numer.* **12**, 399–450 (2003).

36. Hilbert, S., Hänggi, P. & Dunkel, J. Thermodynamic laws in isolated systems. *Phys. Rev. E* **90**(6), 06211 (2014).

37. Rappé, A. K., Casewit, C. J., Colwell, K., Goddard, W. A. III. & Skiff, W. M. UFF, a full periodic Table force field for molecular mechanics and molecular dynamics simulations. *J. Am. Chem. Soc.* **114**(25), 10024–10035 (1992).

38. Lennard-Jones, J. E. Cohesion. *Proc. Phys. Soc. (1926-1948)* **43**(5), 461 (1931).

39. Huray, P. G. *Maxwell's equations*. John Wiley & Sons, (2011).

40. Hayek, S. I. Mechanical vibration and damping. *Digital Encyclopedia of Applied Physics,* (2003).

41. Mueller, M. Fundamentals of quantum chemistry molecular spectroscopy and modern electronic structure computations. *Chemistry in Britain,* (2001).

42. Pounds, A. J. Introduction to quantum mechanics in chemistry (Ratner, Mark A.; Schatz, George C.), Ed: ACS Publications, (2002).

43. Nosé, S. A unified formulation of the constant temperature molecular dynamics methods. *J. Chem. Phys.* **81**(1), 511–519 (1984).

44. Hoover, W. G. Canonical dynamics: Equilibrium phase-space distributions. *Phys. Rev. A* **31**(3), 1695 (1985).

45. Mai, W. *et al.* Prism-based DGTD with a simplified periodic boundary condition to analyze FSS With D 2n symmetry in a rectangular array under normal incidence. *IEEE Antennas Wirel. Propag. Lett.* **18**(4), 771–775 (2019).

46. Hanwell, M. D. *et al.* Avogadro: An advanced semantic chemical editor, visualization, and analysis platform. *J. Cheminform.* **4**(1), 1–17 (2012).

47. Stukowski, A. Visualization and analysis of atomistic simulation data with OVITO–the open visualization tool. *Modell. Simul. Mater. Sci. Eng.* **18**(1), 015012 (2009).

48. Zarringhalam, M. *et al.* Molecular dynamic simulation to study the effects of roughness elements with cone geometry on the boiling flow inside a microchannel. *Int. J. Heat Mass Transf.* **141**, 1–8 (2019)

49. Arefpour, A., Kasiri-Asgarani, M., Monshi, A., Karbasi, S., Doostmohammadi, A., Rostami, S. In vitro bioactivity of baghdadite-coated PCL–graphene nanocomposite scaffolds, mechanism of baghdadite and apatite formation. *Mater. Technol.* 1–10, (2020).

50. Khan, I., Saeed, K., Khan, I. Nanoparticles: Properties, applications and toxicities. *Arab. J. Chem.*, S1878535217300990, (2017).

Acknowledgements

Author contributions

All authors reviewed the manuscript.

Competing interests

The authors declare no competing interests.

Additional information

Correspondence and requests for materials should be addressed to Q.L. or S.B.

Reprints and permissions information is available at www.nature.com/reprints.

Publisher's note Springer Nature remains neutral with regard to jurisdictional claims in published maps and institutional affiliations.